

Study of defect properties and recombination mechanism in rubidium treated Cu(In, Ga)Se₂ solar cells

Cite as: J. Appl. Phys. **129**, 183108 (2021); doi: [10.1063/5.0046098](https://doi.org/10.1063/5.0046098)

Submitted: 1 February 2021 · Accepted: 25 April 2021 ·

Published Online: 13 May 2021



Hamidou Tangara,^{1,a)} Setareh Zahedi-Azad,² Jennifer Not,³ Jakob Schick,² Alban Lafuente-Sampietro,¹ Muhammad Monirul Islam,^{1,4} Roland Scheer,² and Takeaki Sakurai¹

AFFILIATIONS

¹Institute of Applied Physics, University of Tsukuba, Ibaraki 305-8573, Japan

²Institute of Physics, Martin-Luther-Universität Halle-Wittenberg, 06120 Halle, Germany

³Polytech Grenoble, Université Grenoble Alpes, 38400 Saint-Martin-d'Hères, France

⁴Alliance for Research on the Mediterranean and North Africa (ARENA), University of Tsukuba, Ibaraki 305-8573, Japan

^{a)}Author to whom correspondence should be addressed: s2030062@s.tsukuba.ac.jp

ABSTRACT

Heavy alkali-metal treatment of Cu(In,Ga)Se₂ (CIGSe) absorbers has been emerging as a key process for achieving over 23% high conversion efficiencies in CIGSe solar cells. Here, we investigate the effect of rubidium fluoride post-deposition treatment (RbF-PDT) on the electronic and carrier recombination properties of narrow bandgap (narrowgap) and wide bandgap (widegap) CIGSe solar cells using thermal admittance spectroscopy (TAS), transient photocapacitance spectroscopy (TPC), as well as time-resolved photoluminescence (TRPL). We find that the activation energy of the main capacitance step in TAS spectra of narrowgap and widegap CIGSe solar cells reduces after RbF-PDT. On the other hand, capacitance–voltage (*C–V*) and temperature-dependent current–voltage (IVT) measurements demonstrate that the built-in potential, as well as the activation energy *E_a*, increases upon RbF-PDT both for narrowgap and widegap samples, pointing to reduced interface recombination. TPC revealed an appreciable reduction of the optical response of bulk defects in the narrowgap and widegap CIGSe, suggesting improvement of bulk properties after RbF treatment. TRPL confirmed that RbF-PDT significantly reduces carrier recombination in the bulk of narrowgap and widegap CIGSe absorbers and at the surface, leading to extended carrier lifetimes. Analysis of open-circuit voltage (*V_{OC}*) losses due to nonradiative recombination in the bulk of the CIGSe showed a strong correlation between enhanced carrier lifetime and improved *V_{OC}* for narrow gap CIGSe cells. In contrast, although we observed a substantial decrease of *V_{OC}* losses in widegap CIGSe bulk, the analysis indicated that the key to photovoltaic performance enhancement is improved interface quality.

Published under an exclusive license by AIP Publishing. <https://doi.org/10.1063/5.0046098>

I. INTRODUCTION

CuIn_{1–*x*}Ga_{*x*}Se₂ (CIGSe) is a promising semiconductor for the absorber layer of thin-film solar cells. The energy conversion efficiency of such solar cells currently exceeds 23%.^{1,2} The key to practical performance improvements is alkali metals treatment, including rubidium (Rb), Cesium (Cs), potassium (K), and sodium (Na), which is decisive for enhancing the absorber quality and reducing open-circuit voltage (*V_{OC}*) losses.^{3–5} The incorporation of Na into the CIGSe absorbers has been reported as advantageous to increase the hole concentration in the absorber. Due to its small ionic radius, Na accumulates on interstitial sites or diffuses via

Cu-vacancy at interfaces, Cu-deficient grain boundaries, or even into grain interior, resulting in passivation of defects in the CIGSe absorber layer.⁶ On the other hand, K incorporation through post-deposition treatment (KF-PDT) leads most to the enhancement of CIGSe surface properties.⁷ KF-PDT tunes hole concentration and reduces charge carrier recombination in the bulk and at the absorber/buffer interface, which improves the *V_{OC}* and the fill factor (*FF*) of solar cells. Following the recent record efficiency value of 23.35%,¹ CIGSe solar cells with heavy alkali metals PDT, namely, Rb and Cs, have gained much attention. Recent reports revealed that RbF (or Cs)-PDT are more effective than KF-PDT as

they averagely increased the efficiency by $\sim 2.42\%$,⁸ an improvement linked to the substantial increase of V_{OC} and FF . Many experimental and theoretical studies have been undertaken to explain the reasons for improved efficiency. Increased carrier concentration,^{9,10} improved CIGSe/CdS interface quality due to the formation of Rb-related compound (e.g., RbInSe_2),¹¹ and bulk defects passivation are commonly proposed;¹² however, full understanding is still lacking.

Widgap CIGSe are increasingly regarded as the most desirable solution to achieve the optimum energy conversion efficiency theoretically calculated at $E_g = 1.4$ eV, improve the photovoltaic (PV) performance of CIGSe solar cells under real operating conditions,² and build multi-junction thin-film widgap CIGSe on silicon solar cells with considerably high conversion efficiencies. Nevertheless, incremental Ga content beyond GGI ($\text{GGI} = (\text{Ga}/[\text{In} + \text{Ga}])$ of 0.3 to adjust bandgap energy usually causes degradation of the CIGSe absorber quality, leading to low collection efficiency and saturation of V_{OC} .^{4,5} Similar to narrow gap CIGSe, heavy alkali metals have been introduced into widgap CIGSe absorbers to improve device efficiency.^{13,14} RbF-PDT has been found to be effective for minimizing the V_{OC} deficit and interface recombination in these materials.¹³ However, a comparative study of the effect of RbF-PDT on the electronic properties of narrowgap and widgap CIGSe solar cells fabricated under similar experimental conditions has not yet been discussed, which limits our understanding of the role of RbF-PDT in improving the efficiency of CIGSe solar cells. In this contribution, we used temperature-dependent current-voltage (IVT) measurement, junction capacitance-based techniques such as thermal admittance spectroscopy (TAS), and transient photocapacitance spectroscopy (TPC) along with time-resolved photoluminescence (TRPL) measurements to investigate the impact of RbF-PDT on the shallow and deep-level defects properties in narrowgap and widgap CIGSe.

II. MATERIALS AND METHODS

A. Sample processing

CIGSe absorbers with different Ga contents were prepared by a previously reported multi-stage growth process.^{13,14} Briefly, CIGSe absorbers of about $2.5\ \mu\text{m}$ thick were deposited on Mo coated soda-lime glass substrates using a four-source elemental evaporation system. Ga content $[\text{Ga}]/([\text{Ga}] + [\text{In}])$ (or GGI) was controlled to be 0.30, 0.60, and 0.73, as determined by energy-dispersive x-ray spectroscopy. The post-deposition treatment was performed using RbF under Se atmosphere. The RbF was evaporated with a rate of $0.1\ \text{\AA/s}$ for about 32 min at a substrate temperature of 725 K. CIGSe absorber films without RbF treatment were also prepared and will serve as control samples. All devices were finished by 50 nm thick CdS deposited by chemical bath and then rf-sputtering of an undoped ZnO layer and doped ZnO: Al layer. A Ni/Al/Ni grid was then deposited with an electron beam to form the top contact.

B. Characterization

To investigate the electrically active defects, we measured dark thermal admittance spectra (TAS) of CIGSe devices in the

temperature range of 50–340 K using Agilent 4284 A LCR meter with ac frequencies from 1 kHz to 1 MHz and 25 mV of modulation voltage. Measurements were conducted in a vacuum cryostat, cooled by liquid nitrogen flow through the surrounding jacket. The system was equipped with a thermometer and a heater to precisely control the sample temperature.

Capacitance-voltage ($C-V$) measurements were performed at room temperature on the same system. Before each measurement, samples were heated at 320 K for about 30 min and then allowed to relax in the dark for at least 10 h. This heating step is important to avoid the contribution of metastable states of the samples.

As for transient photocapacitance measurements (TPC), a monochromator equipped with a tungsten-halogen white light source ranging from 680 to 1800 nm, and optical mode sorting filters was used. Spectra were acquired using a Boonton 72B capacitance meter with a filling voltage of 0 V and a quiescent bias of -0.5 V. The electrical pulse width and duration were set at 50 ms and 1 s, respectively. The transient response, which emerges following the voltage filling pulse, was integrated over a fixed time window of 750 ms using an analog-to-digital converter with a fixed rate window of $2\ \text{s}^{-1}$.

Time-resolved photoluminescence (TRPL) measurements were carried out using a femtosecond Ti-sapphire laser. Transients were recorded on CdS covered CIGSe films where the light spot size on the sample was about $40\text{--}80\ \mu\text{m}$. For excitation, a pulsing laser source with a repetition rate and pulse width of 2 MHz and ~ 80 fs, respectively, was used. For detection, we used an InGaAs-based photomultiplier tube (Hamamatsu H10330A-75) and an avalanche photodiode detector (IDQ ID-100) with a sensitivity range of 300–900 nm and 40 ps time resolution. The decay curves were measured at the peak energy of the corresponding PL emission. All TRPL measurements were carried out at room temperature (RT).

III. RESULTS AND DISCUSSION

A. Photovoltaic performance

The PV parameters of $\text{ZnO:Al/i-ZnO/CdS/CIGSe/SLG}$ heterostructure devices used in the current study are listed in Table I. The corresponding $J-V$ characteristics are shown in Fig. S1 in the supplementary material.

As seen from the table, RbF-treated samples show a higher V_{OC} , short circuit current density (J_{SC}), and FF compared to the untreated ones, resulting in improved conversion efficiency. Upon treatment, we observed a remarkable improvement of J_{SC} for widgap CIGSe solar cells. This effect has also been observed in KF-PDT and Cs-PDT cases.¹⁵ An increase of EQE in the long-wavelength region may be one of the origins of higher J_{SC} .

B. Admittance spectroscopy measurements

At first, we studied RbF-treated and untreated CIGSe solar cells with different GGIs by TAS in a temperature range of 50–340 K in the dark and at zero bias voltage. All samples showed a single capacitance step in the measurement temperature range. The activation energies of the observed capacitance steps were determined from the slope of the Arrhenius plot of temperature-

TABLE I. PV properties of untreated (no-PDT) and RbF-treated CIGSe solar cells with different Ga contents, GGI (=Ga/[In + Ga]) 0.30, 0.60, and 0.73, measured under AM 1.5 illumination at room temperature.

Ga content	J_{SC} (mA cm ⁻²)		V_{OC} (mV)		FF		Efficiency (%)	
	No-PDT	RbF-treated	No-PDT	RbF-treated	No-PDT	RbF-treated	No-PDT	RbF-treated
0.30	32.2	33.0	665	684	75.7	76.0	16.2	16.9
0.60	19.5	24.0	737	814	71.4	74.0	9.8	14.0
0.73	17.0	20.2	730	866	63.1	71.0	7.8	12.4

dependent characteristic frequencies ω_0 [i.e., $\ln(\omega_0/T^2)$ vs $1/T$] following Eqs. (1) and (2):¹⁶

$$\omega_0 = \xi_0 T^2 \exp\left(-\frac{E_a}{k_B T}\right), \quad (1)$$

$$\xi_0 T^2 = 2 N_{c,v} v_{th} \sigma_{n,p}, \quad (2)$$

where ω_0 denotes the characteristic frequency of the capacitance step. ξ_0 is the thermal emission pre-factor. $N_{c,v}$ is the effective density of states in the valence or conduction band. v_{th} is the thermal velocity, and $\sigma_{n,p}$ is the hole/electron capture cross section.

The obtained Arrhenius plots are depicted in Fig. S2 in the [supplementary material](#). To get a better insight into the capacitance step in the TAS spectra, we calculated the derivative of capacitance with respect to the angular frequency of the ac applied voltage at the space charge region (SCR) after Walter *et al.*¹⁶ (see Fig. 1). The calculated activation energies are also shown in Fig. 1.

As it can be seen, the activation energies of no-PDT samples are 101, 112, and 120 meV for GGI equal to 0.3, 0.6, and 0.7, respectively. RbF-treated samples showed relatively low activation energies ranging from 58, 61, and 78 meV for GGI equal to 0.3, 0.6, and 0.7, respectively. The integral defect densities obtained by fitting the distribution to a Gaussian function over the energy-scale do not show significant change between RbF-treated and untreated samples.

Furthermore, the thermal emission pre-factor of the observed capacitance step in all CIGSe samples obeys the Meyer-Neldel (MN) rule for thermally activated processes (or compensation law).¹⁷ We observed almost a linear relationship between the thermal emission pre-factor ξ_0 and the activation energies E_a (Fig. 2). For this reason, it is expected the capacitance steps arise from the same origin. Given that Eq. (1) neglects the thermodynamic entropy (which can be significant in CIGSe¹⁸), it is somewhat inaccurate to assign the capacitance step only from TAS data. Nevertheless, the observed activation energies are in the same range as typical values of the N1 signature reported in the literature.^{19,20} The origin of the N1 signature has been widely discussed in the literature. Interface defects,²⁰ bulk defects,²¹ potential barriers in the windows stack,^{22,23} or a defective barrier at Mo/CIGSe back contact^{19,24} are commonly proposed.

In the current study, to understand the origin of the observed capacitance step, we measured IVT characteristics in the temperature range of 80–310 K. As shown in Fig. 3, the RbF-treated samples exhibit rollover characteristics of the J - V curves in the low-

temperature region from 80 to 170 K for GGI equals 0.3 and 0.6. This suggests the presence of a backside potential barrier for the charge carriers, resulting in the blocking of the diode current for RbF-treated samples. If the capacitance step originated from the barrier at the back contact, as suggested by some studies,^{19,24} corresponding activation energy of the step should be related to the height of the barrier. We modeled the back contact as a Schottky barrier with a height ϕ_B using the double diode concept proposed in Refs. 24 and 25 (Fig. S3 in the [supplementary material](#)). Following the model proposed in Ref. 25, the **total series resistance** was expressed as

$$R_S = R_0 + \frac{k}{qA^*T} \times \exp\left(\frac{\phi_B}{k_B T}\right), \quad (3)$$

where A^* is the effective Richardson constant and R_0 the background resistance is assumed to be weakly dependent on temperature. The values of ϕ_B can then be determined from a plot of $\ln(R_S T)$ vs $1/T$. The extracted values of ϕ_B for RbF-treated and untreated samples are displayed in Fig. S4 in the [supplementary material](#). In general, the observed values of ϕ_B are lower than the activation energy of the capacitance step in TAS. Moreover, the obtained values do not follow the trend of the activation energy upon RbF-PDT, likely indicating that the observed capacitance step in these samples arises due to a barrier at the CdS/CIGSe interface.

C. Temperature-dependent dark J - V and C - V analyses

To further make a quantitative analysis about the effect of RbF treatment on the CIGSe absorber layers and fabricated devices, we studied the dominant recombination mechanism in the different devices from the calculation of the activation energy E_a of the reverse saturation current density, J_0 . J_0 has been determined from the diode current,²⁶

$$J_{diode} = J_0 \exp\left(\frac{qV}{Ak_B T}\right) = J_{00} \exp\left(\frac{-E_a}{Ak_B T}\right) \exp\left(\frac{qV}{Ak_B T}\right), \quad (4)$$

where J_{00} is a reference current density with is nearly temperature independent. E_a is the activation energy of J_0 and A is the diode ideality factor. E_a can then be determined using the following expression:

$$\ln\left(\frac{J_0}{J_{00}}\right) = \frac{-E_a}{A(T)k_B T}. \quad (5)$$

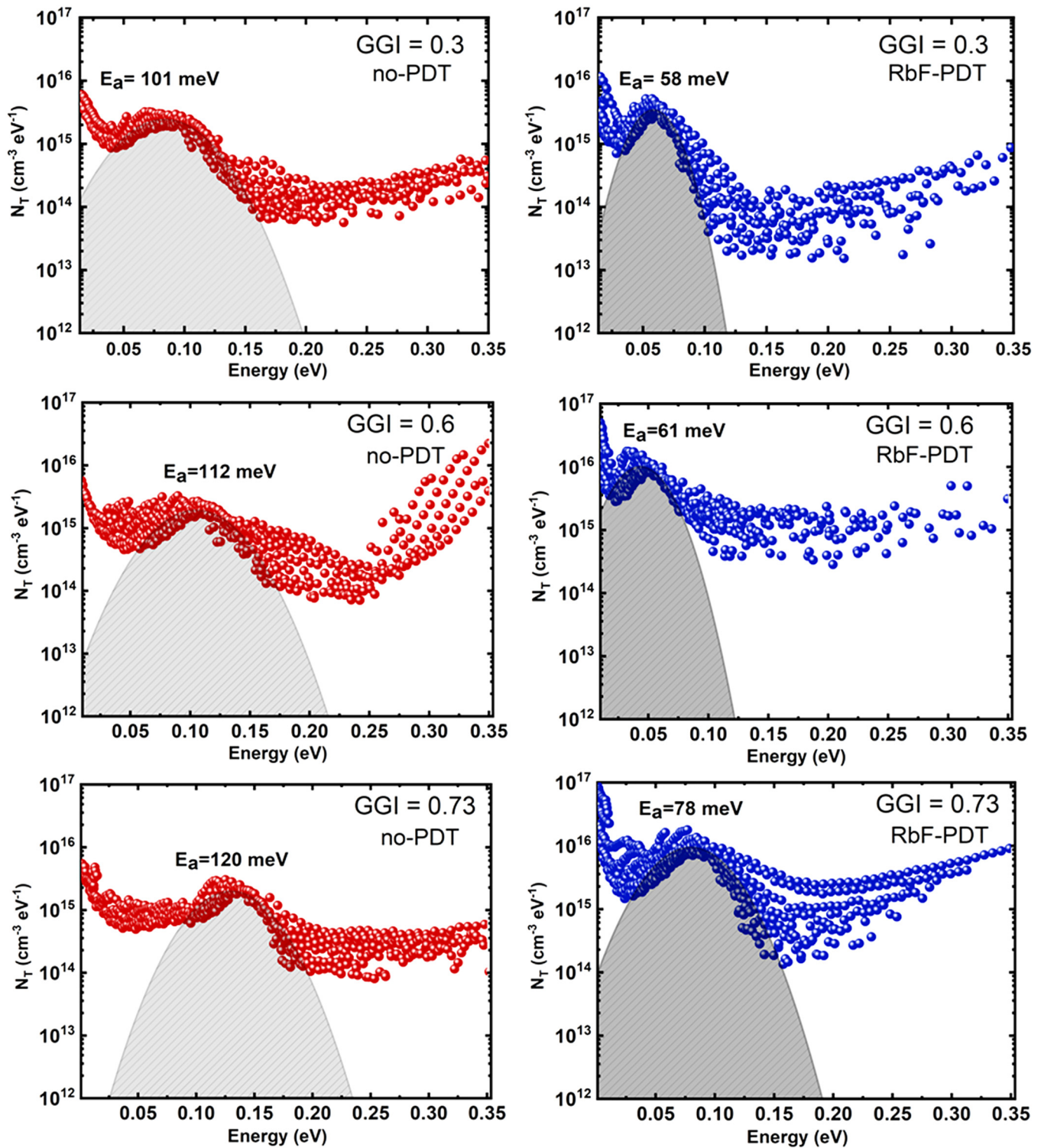


FIG. 1. Density of defect states, N_T , as a function of energy obtained from admittance spectra of untreated (no-PDT) and RbF-treated (RbF-PDT) CIGSe solar cells with different Ga contents: GGI 0.30, 0.60, and 0.73. The shaded portions indicate data fit with a Gaussian-shaped band.

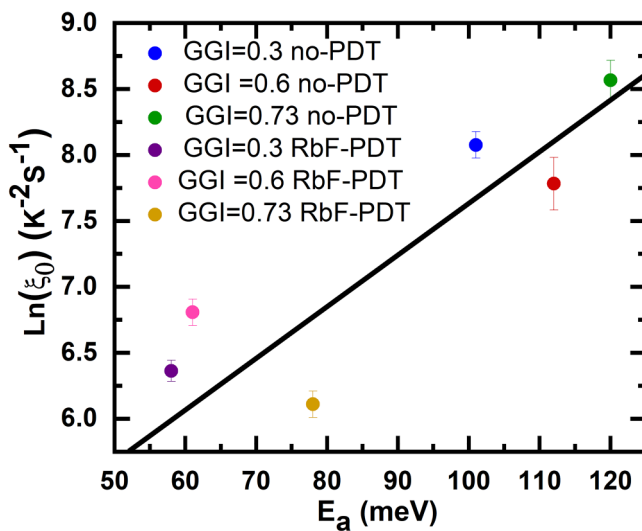


FIG. 2. Meyer-Neldel plot of pre-exponential factor ξ_0 and activation energies E_a extracted from the Arrhenius plots of characteristic frequencies obtained from admittance spectra of untreated (no-PDT) and RbF-treated (RbF-PDT) CIGSe solar cells with different Ga contents: GGI 0.30, 0.60, and 0.73.

In the case of E_a equals to the absorber bandgap E_g , the device is considered to be dominated by recombination in the space charge region. On the other hand, in devices where the CdS/CIGSe interface recombination dominates, such as widegap CIGSe,²⁷ E_a is expected to be lower than E_g . Tables II and III summarized the activation energy and the bandgap for the different samples [see Fig. S5 in the [supplementary material](#) for plots of $A \cdot \ln(J_0)$ vs; $1/k_B T$].

As shown in the table, in the case of untreated samples, calculated activation energy seems to be closer to the bandgap of the narrowgap CIGSe, while the value of activation energy becomes smaller comparing to the bandgap widegap CIGSe (GGI = 0.6 and 0.73). The results suggest that the interface recombination is less severe untreated narrowgap sample, whereas interface recombination plays a major role in widegaps, consistent with previous reports.¹⁵

Upon RbF-PDT, the activation energy becomes equal to the bandgap energy of the narrow gap CIGSe, suggesting a shift of the dominant recombination process from interface to bulk recombination. In the widegap CIGSe, we observe an increase in the activation energy, which implies that the interface recombination was reduced after PDT. However, the activation energy remains smaller than the bandgap energies of these materials, indicating the dominance of interface recombination.

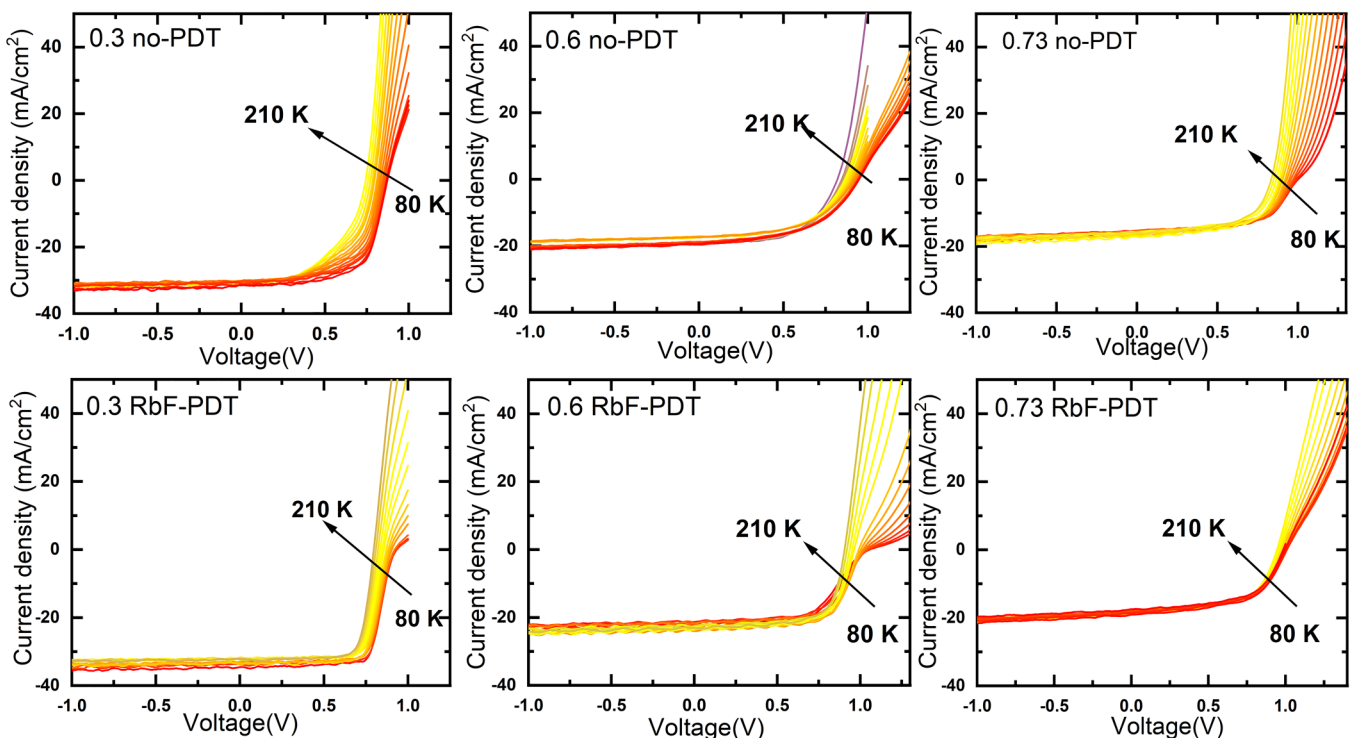


FIG. 3. Temperature dependence of the J - V curve of RbF-treated (RbF-PDT) and untreated (no-PDT) CIGSe solar cells with different Ga contents: GGI 0.30, 0.60, and 0.73 in the temperature range of 80–210 K.

TABLE II. Activation energy, E_a , and bandgap for RbF treated and untreated. The bandgap values were determined by plotting $[E \times \ln(1 - EQE)]^2$ vs E curves, where E is the photon energy.²⁸

	0.30		0.60		0.73	
	Untreated	RbF-treated	Untreated	RbF-treated	Untreated	RbF-treated
E_a (eV)	0.95 ± 0.02	1.13 ± 0.02	0.91 ± 0.02	1.25 ± 0.04	0.93 ± 0.02	1.4 ± 0.03
E_g (eV)	1.19	1.19	1.33	1.34	1.48	1.46

Furthermore, Fig. 4 shows the built-in potentials, V_{bi} , obtained by a linear fitting of the Mott-Schottky plots ($1/C^2 - V$) (see Fig. S6 in the [supplementary material](#)), as a function of Ga content. As seen in the figure, V_{bi} drastically increases for RbF-treated widegap samples (i.e., GGI = 0.60 and 0.73), while no noticeable change is observed for the narrow sample (GGI = 0.3). These results suggest that RbF-PDT modifies the CdS/CIGSe interface plausibly by forming a RbInSe₂ interfacial layer.²⁹ Such an interfacial layer could reduce interface recombination, which leads to improved V_{OC} and eventually high conversion efficiencies.

D. Transient photocapacitance spectroscopy measurements

In order to investigate the optically active sub-bandgap defect states in the CIGSe absorber, we measured the TPC signals at a low temperature of 120 K. The CIGSe junction was biased with a negative voltage of -0.5 V. A voltage pulse with a magnitude of $+0.5$ V and a width of 50 ms was then applied to fill the traps in the SCR by charge carriers. After returning to reverse bias of -0.5 V, the traps above the Fermi level re-emitted the previously captured carriers to the band edges. Those carriers can move out of the SCR due to the influence of the electrical field. As these carriers escape from the SCR, a change in the junction capacitance produces the transient capacitance signal. In the dark, this process is primarily driven by thermal excitation. However, this emission process can be enhanced through optical excitation. The difference between transient signals measured in the presence of monochromatic light and those in the dark, normalized to the photon flux, yields the TPC signal,

$$S_{\text{TPC}} = \frac{\int_{t_1}^{t_2} C_{\text{light}}(t)dt - \int_{t_1}^{t_2} C_{\text{dark}}(t)dt}{\text{Photon flux}}. \quad (6)$$

TABLE III. Fitted TRPL parameters for CIGSe absorbers with GGI = 0.3. TRPL transients were measured using different excitation wavelengths (400 and 750 nm). Carrier lifetimes were extracted using a double exponential fit.

Ga content	Alkali treatment	Minority carrier lifetimes (ns)			
		400 nm		750 nm	
		τ_1	τ_2	τ_1	τ_2
0.30	Untreated	8.3	36.7	10	39
	RbF-treated	10.3	53.4	12	50

The entire TPC signals were recorded as a function of the monochromatic light wavelength. Shown in Fig. 5 are TPC spectra of narrowgap and widegap CIGSe samples before and after RbF-PDT. TPC signals are normalized to their maximum values above the bandgap energy so that the maximum amplitude is 1. We note that all TPC spectra were recorded at the same temperature. Thus, the effect of variation of the thermal emission rate of the trapped holes from the defect band due to change of temperature is eliminated.

We observed a broadening of the sub-bandgap spectra with increasing Ga content, which is likely due to the strong electron-phonon coupling for deep-level traps in widegap samples.³⁰

A steep increase of the TPC signal intensity is also observed in the interband absorption region with increasing photon energy for all samples, which can be ascribed to the large cross sections of band-to-band optical transitions.

Moreover, the magnitude of the shoulders below ~ 1.1 eV significantly decreases after RbF-PDT for narrowgap and widegap samples, plausibly indicating a reduction of bulk defects density with the incorporation of Rb. That is, while the filling ensures that most trap states are filled with holes, the TPC spectrometer records the optical excitation of holes out of these states. Since the TPC signal is proportional to the number of emitted holes, which, in turn, is related to the density of trap states within the bandgap, a decrease of the intensity of the TPC signal indicates a reduced trap state density.

The quantitative analysis of TPC for RbF-treated and untreated samples could not be performed with high accuracy as such an analysis can only be done in steady-state conditions.³¹ However, we note that the decrease of the TPC intensity correlates well with the increase of V_{OC} after RbF-PDT.

Possible origin of the sub-bandgap absorption has been primarily considered as point defects and defect complexes³² such as In_{Cu} , Ga_{Cu} ,³³ and $(\text{In}_{\text{Cu}}, \text{Ga}_{\text{Cu}}) + 2V_{\text{Cu}}$ ³⁴ present within the grains and at the grain boundaries. Although our previous study could not confirm definitive relation between deep levels observed by TPC and Se-dependence,³⁵ considering the amphoteric nature of Se-vacancy related complex suggested by several groups,^{36,37} role of Se-related defects cannot be ruled out as one of the possible origins for bulk defects. Nevertheless, the reduced optical response in the sub-bandgap region after PDT suggests the reduction of the density of deep-level defects. Due to their large ionic radii, the Rb atoms are unlikely to occupy the V_{Cu} ; the high formation energy of compensating antisite Rb_{Cu} supports this conjecture.³⁸ However, the formation of a RbInSe_2 compound at the grain boundaries, where a relatively low chemical potential exists and atoms are loosely

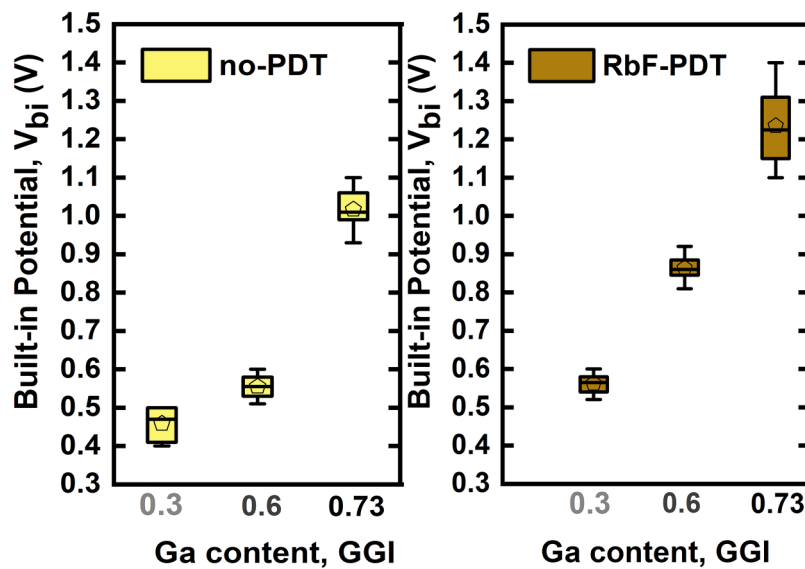


FIG. 4. Built-in potential (V_{bi}) obtained from C–V spectra of RbF-treated (RbF-PDT) and untreated (no-PDT) CIGSe solar cells with different Ga contents, GGI (=Ga/[In + Ga]) 0.30, 0.60, and 0.73.

arranged,³⁹ may roughly explain this reduction in sub-bandgap defects density. These findings suggest that RbF treatment improves V_{OC} of CIGSe solar cells by reducing bulk defect density.

E. Time-resolved photoluminescence measurements

Next, we investigated whether RbF-PDT also affects the minority carrier lifetimes. At first, we have measured TRPL decays as a function of excitation wavelength to distinguish interface and bulk recombination in the CIGSe absorbers. Shown in Fig. 6 are room temperature TRPL spectra of CdS/covered CIGSe with GGI = 0.3 measured at 1030 nm using two different excitation wavelengths, namely, 750 and 400 nm. The excitation intensities were tuned to be weak enough such that (i) the radiative emission lifetimes are independent of illumination intensity and (ii) the measurement conditions correspond roughly to 1 sun illumination condition (assuming a spatially uniform distribution of carriers in the absorber). On the other hand, the penetration depth of excitation wavelengths was determined from the absorption coefficient⁴⁰ of CIGSe material with GGI = 0.3 found as 291 nm and 50 for 750 and 400 nm excitation wavelength, respectively. The photon density, I_{ex} , per pulse was 6.3×10^{10} photons cm^{-2} pulse⁻¹ for 750 nm and 2.4×10^{10} photons cm^{-2} pulse⁻¹ for 400 nm excitation laser source.

To extract carrier lifetimes, we fitted TRPL curves to a double exponential function,

$$I(t) = C_1 \exp\left(\frac{-t}{\tau_1}\right) + C_2 \exp\left(\frac{-t}{\tau_2}\right), \quad (7)$$

where t is the time after an excitation pulse, C_1 and C_2 are fitting constants, τ_1 and τ_2 are the fast and slow decay lifetimes, respectively. Table II summarizes the fitted TRPL parameters of CIGSe samples with GGI = 0.30 before and after RbF-PDT. (Table S1 in the supplementary material summarizes the fitted TRPL

parameters for all the samples.) Both fast and slow decay lifetimes, i.e., τ_1 and τ_2 , change with excitation wavelength, but the extent is slightly greater for τ_1 . Figures 6(b) and 6(c) show the fast decay changes as a function of excitation wavelength in the first 10 ns for CIGSe samples with GGI = 0.30 before and after RbF-PDT. The fast decay component strongly depends on the penetration depth of the excitation wavelength. For 750 nm, extended lifetimes are measured, whereas 400 nm excitation wavelength produces short lifetimes. The effect can be understood if surface recombination is considered. For 400 nm, the excitation depth is near to the surface, hence surface properties strongly affect the fast decay component. To this end, τ_1 can be attributed to surface recombination, and the slow decay component τ_2 can be related to bulk recombination. Comparison of RbF-treated sample to untreated one reveals that RbF-PDT reduces surface recombination in CIGSe absorber. On the other hand, due to the relatively higher injection level near the surface, τ_1 might be affected by other surface processes including charge separation,⁴¹ bimolecular recombination,⁴² and the laser onset. For the 400 nm excitation, considering photon density and absorption coefficient, α at 400 nm, the injection level has been estimated as $\sim 5 \times 10^{15}$ photon pulse⁻¹ cm^{-3} . The injection level is nearly in the same order of magnitude as the effective carrier density ($\sim 10^{16}$ cm^{-3}). In this case, surface processes reduce the number of carriers participating in the recombination process, leading to shorter τ_1 values. In contrast, the carrier generation occurs deeper in the absorber bulk when excited with a 750 nm laser source, resulting in longer surface lifetimes than those measured with 400 nm in the same sample. Nevertheless, we observe an improvement of carrier lifetimes in all samples for both excitation wavelengths. Our analysis suggests that surface properties of CIGSe absorbers are enhanced after RbF-PDT. The effect is qualitatively the same for widegap samples, but the extent is slightly lower for them (see Fig. S7 in the supplementary material). A possible interpretation of the effect is the initial high surface recombination of the widegap CIGSe.

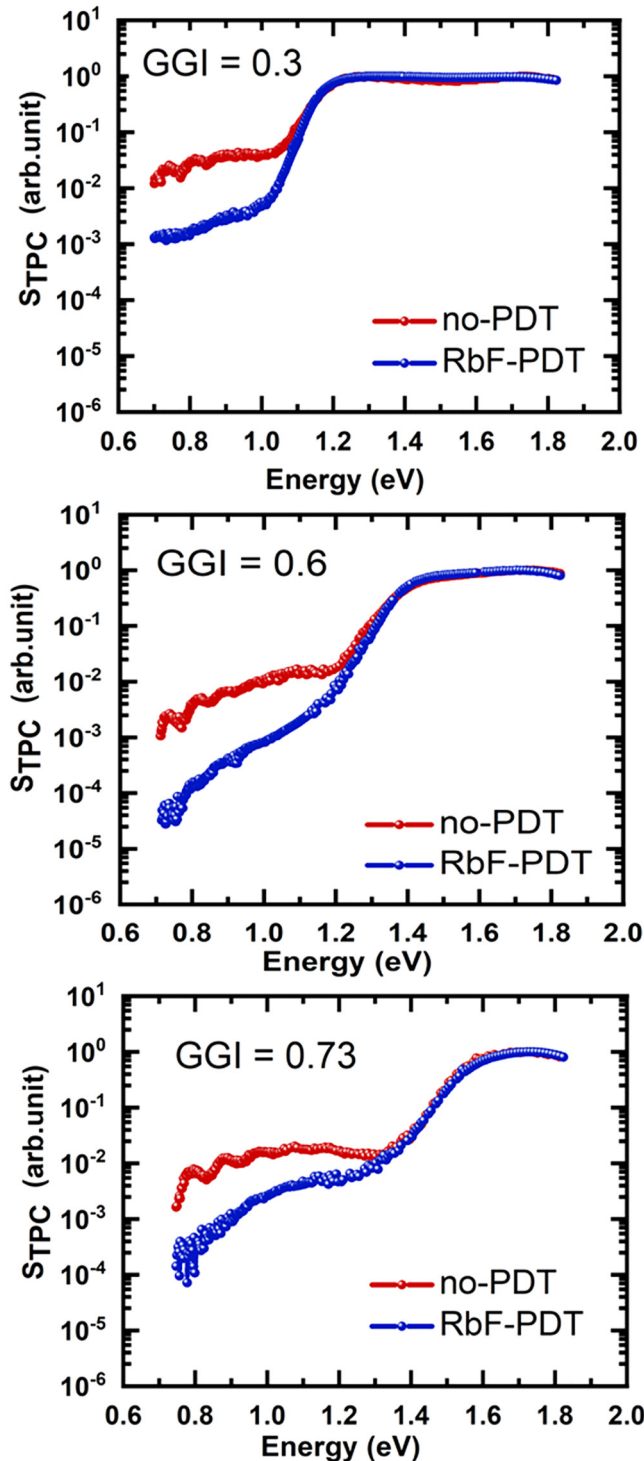


FIG. 5. TPC signals measured at 120 K for untreated (no-PDT) and treated (RbF-PDT) CIGSe solar cells with different Ga contents, GGI (=Ga/(In + Ga)) 0.30, 0.60, and 0.73.

To investigate the effect of RbF-PDT on carrier recombination in more detail, TRPL transients of CdS covered CIGSe absorbers with different Ga contents before and after RbF-PDT measured with 750 nm were examined (Fig. 7). We will focus our discussion on bulk recombination; thus, only τ_2 is considered. The τ_2 values obtained from the double exponential fitting of TRPL curves are shown in the figure. Considering that τ_2 is more related to carrier recombination in the bulk of CIGSe absorbers, the results indicate that bulk recombination in widegap CIGSe is higher than that of narrow gap CIGSe, consistent with previous findings.^{41,43} Interestingly, carrier lifetimes substantially increased with RbF-PDT suggesting reduced bulk recombination. So far, all the measured lifetimes were in the order of nanoseconds, which is far behind the ideal radiative lifetime, $\tau_{\text{rad,ideal}}$ (of few microseconds) estimated theoretically using the van Roosbroek–Shockley relation. The ideal radiative lifetime, $\tau_{\text{rad,ideal}}$ calculated as $\tau_{\text{rad,ideal}} = (BN_A)^{-1}$ ⁴⁴ under low injection conditions, is different for each set of samples because both effective carrier density, N_A , and radiative recombination constant, B , change with Ga content. Furthermore, a change of the ideal radiative lifetime is also expected even for the same set of samples with the same GGI value due to the increase of N_A and possibly the radiative recombination constant upon treatment. Table S2 in the [supplementary material](#) summarizes the radiative recombination constants (estimated using the Van Roosbroek–Shockley relation), N_A obtained from C–V measurements, and ideal radiative lifetimes for all samples. The PL lifetimes can be expressed as a function of radiative carrier τ_{rad} and nonradiative lifetimes τ_{nr} as $\tau_{\text{PL}} = 1/\tau_{\text{rad}} + 1/\tau_{\text{nr}}$. Thus, the results suggest that the measured lifetime is the nonradiative lifetime ($\tau_{\text{PL}} \approx \tau_{\text{nr}}$ for $\tau_{\text{nr}} \ll \tau_{\text{rad}}$), which means that carrier recombination in the CIGSe bulk predominately occurs via nonradiative transitions, presumably via deep-level traps [i.e., Shockley–Read–Hall (SRH) recombination]. The minority carrier (electron) lifetime for SRH recombination can be expressed as

$$\tau_{\text{nr}} = \frac{1}{\nu_{\text{th}} \sigma_e N_t}. \quad (8)$$

Here σ_e is the capture cross section of electrons and N_t is the density of traps.

For the sake of simplicity, we assume that σ_e and ν_{th} do not change with RbF-PDT.⁴⁵ Accordingly, Eq. (8) suggests that RbF-PDT decreases the density of defects in the CIGSe bulk, resulting in longer lifetimes. Due to the strong electron–phonon interactions at deep levels, the deep traps usually provide an efficient pathway for carrier recombination. Thus, TRPL results suggest that RbF-PDT significantly improves the bulk properties. This finding is consistent with the observed reduction of TPC signal from bulk defects upon RbF-PDT. Alternatively, reduced recombination at the grain boundaries due to the accumulation of Rb could increase carrier lifetime.^{10,12,38}

The long minority carrier lifetimes are associated with large diffusion lengths L_n ($L_n \propto \sqrt{\tau_n}$), resulting in higher collection efficiencies from the backside in RbF-treated CIGSe than untreated ones.

To correlate the improvement of PV performance with the enhancement of electronic properties of CIGSe absorbers, we

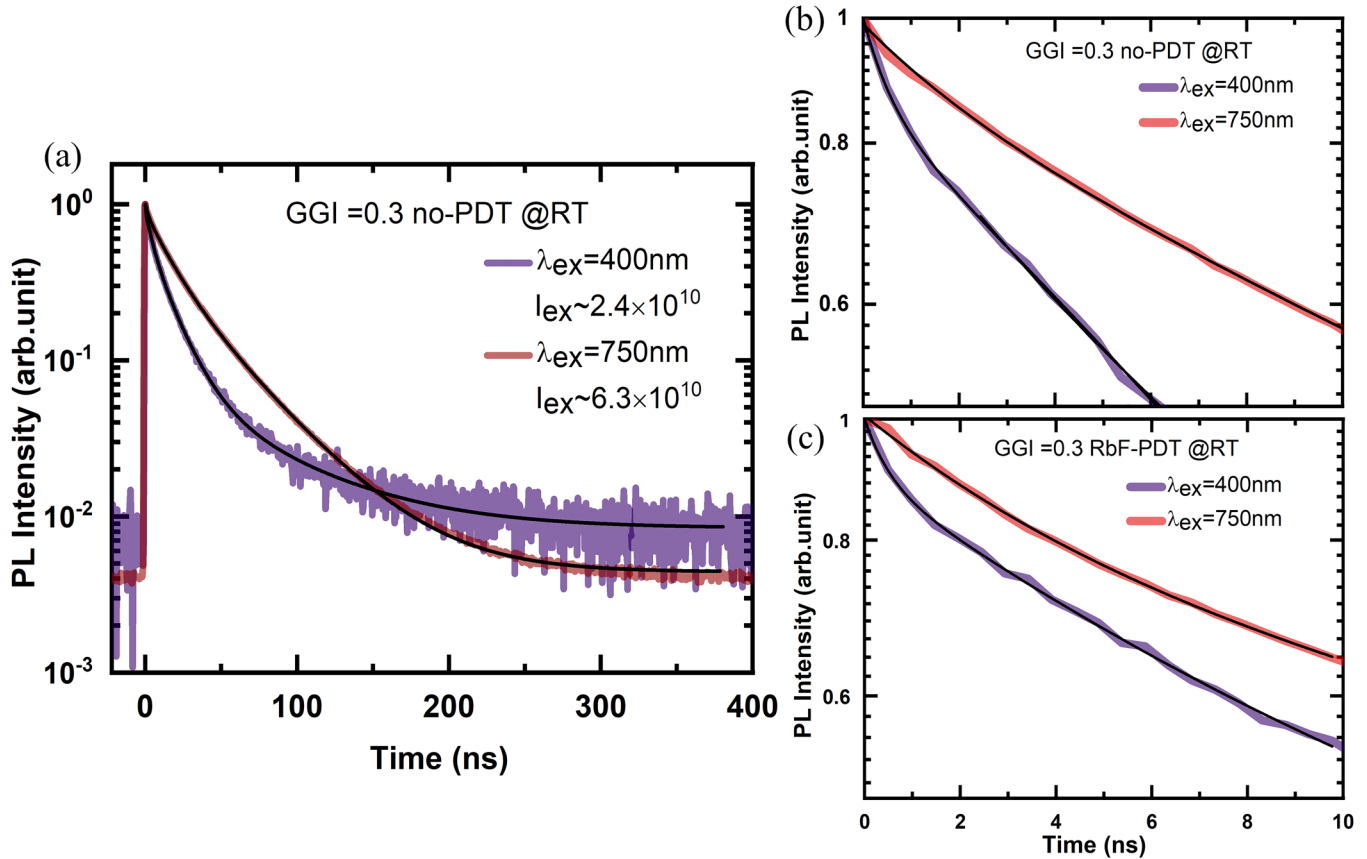


FIG. 6. (a) Wavelength-dependent RT TRPL curves of untreated (no-PDT) CdS covered CIGSe solar cells with GGI = 0.3. Changes in the fast decay times, τ_1 , in the first 10 ns (b) untreated and (c) RbF-treated (RbF-PDT) samples with GGI = 0.3. The black lines are double exponential fitting. The unit of photon density I_{ex} is photon pulse⁻¹ cm⁻².

calculated the V_{OC} losses due to nonradiative recombination. Following Werner *et al.*⁴⁶ and later works, we estimated the ideal saturation current density, $J_{0,ideal}$, in the limit of radiative recombination assuming a thin-film sample,

$$J_{0,ideal} = \frac{qWn_i^2B}{n_r^2} = \frac{qWn_i^2}{n_r^2} \left(\frac{1}{\tau_{rad,ideal}N_A} \right). \quad (9)$$

Here, W is the film thickness ($W = 2.5 \mu\text{m}$), n_r is the refractive index ($n_r = 3$), and n_i is the intrinsic carrier concentration, which can be calculated using the bandgap energy values. For the non-ideal case, we introduced the measured PL lifetimes τ_{PL} in Eq. (9) to calculate the saturation current density ($J_{0,rad}$). Finally, we estimated the V_{OC} losses due to nonradiative recombination using the following equation:⁴⁷

$$\Delta V_{OC} = \frac{k_B T}{q} \ln \left(\frac{J_{0,ideal}}{J_{0,rad}} \right). \quad (10)$$

The CIGSe solar cells have a high nonradiative recombination loss, in particular, for widegap absorbers. Thus, this analysis seems convenient to understand how RbF-PDT reduces the V_{OC} loss. Here, we primarily considered nonradiative recombination occurring in the bulk by using τ_2 values in Eq. (9). Table S3 in the [supplementary material](#) gives the results of calculation for samples with GGI = 0.3 (narrowgap) and GGI = 0.73 (widegap). Upon RbF-PDT, a reduction of about 25 mV in the V_{OC} loss is calculated for samples with GGI = 0.3. In contrast, the V_{OC} loss due to bulk recombination decreases by about 32 mV for GGI = 0.73. The higher reduction of V_{OC} loss in widegap CIGSe compared to narrowgap case reflects the greater enhancement of their bulk properties after RbF-PDT. These values were compared to the experimentally observed increase of V_{OC} with RbF-PDT to quantify the impact of bulk properties on the PV performance of narrowgap and widegap devices. As it can be seen from [Tables I](#) and [S3](#) in the [supplementary material](#), V_{OC} improvement of 19 mV is measured for samples with GGI = 0.3, which agrees well with the calculated value. The result implies that the enhancement of bulk properties is the key to PV performance improvement for narrow gap CIGSe

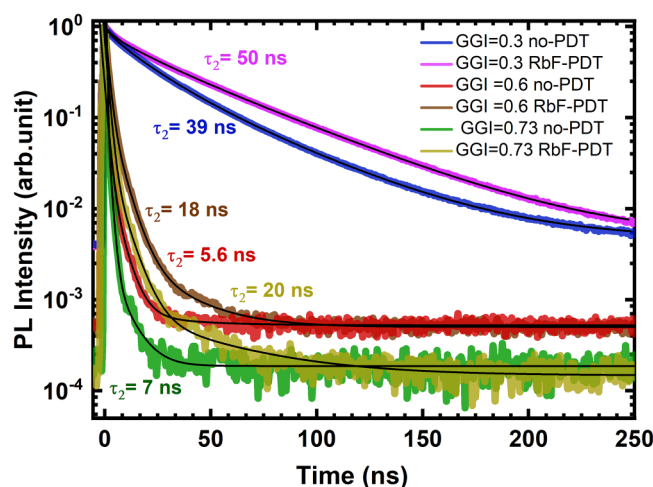


FIG. 7. RT TRPL curves for untreated (no-PDT) and RbF-treated (RbF-PDT) CIGSe solar cells with different Ga contents, namely, GGI (=Ga/[In + Ga]) 0.30, 0.60, and 0.73. The excitation wavelength was set to 750 nm with excitation density $\Delta n \sim 10^{15}$ photon pulse $^{-1}$ cm $^{-3}$. The black lines are double exponential fitting. τ_2 are the slow decay component.

solar cells. However, the V_{OC} improvement measured for the widegap sample (GGI = 0.73) of 136 mV after treatment is significantly higher than the calculated one. Such a result reinforces that the major contribution to PV performance improvement for widegap CIGSe solar cells upon RbF treatment is the enhancement of interface properties. This conclusion is consistent with the dark J - V analysis.

Our analysis shows that for widegap CIGSe solar cells, RbF-PDT plays a significant role in improving interface properties, leading to reduced V_{OC} loss. While improvement of bulk properties after RbF-PDT accounts for the most improvement of PV performance in the narrow gap CIGSe solar cells case.

IV. CONCLUSION

We presented a study of the electronic and carrier recombination properties of narrowgap and widegap CIGSe solar cells before and after RbF-PDT. The activation energy of the main capacitance in TAS spectra decreases with RbF-PDT for narrowgap and widegap samples, as well as the built-in potential (V_{bi}) and the activation energy of the dominant recombination increases after the treatment, pointing to reduced interface recombination. Moreover, TPC measurements indicate a reduction of bulk defects optical response after RbF-PDT for both narrowgap and widegap samples, suggesting improvement of bulk properties of CIGSe absorbers. Carrier recombination study using wavelength-dependent TRPL indicates a reduction of CdS/CIGSe interface recombination along with a decrease of bulk defect density after RbF treatment for all samples. The extent is greater for widegap samples, likely due to their initial high carrier recombination rates. Enhanced carrier lifetimes in the bulk correlates well with the observed improvement of V_{OC} in narrowgap CIGSe solar cells after RbF treatment. In

contrast, the carrier lifetime enhancement only partially explains the PV performance improvement in widegap devices. Our analysis suggests that RbF-PDT is most efficient to improve both bulk and interface properties of CIGSe absorbers with a relatively significant contribution due to reduced interface recombination in widegap CIGSe solar cells.

SUPPLEMENTARY MATERIAL

See the [supplementary material](#) for the following plots [J - V curves, Arrhenius plots of characteristic frequencies, Mott-Schottky ($1/C^2$ vs V), the total series resistance [$\ln(R_s T)$ vs $1/T$], activation energy E_a of J_0 , changes in the fast decay times of the different wavelengths for the samples with GGI = 0.6 and 0.73], and a summary of the TRPL decay lifetimes, ideal radiative lifetimes, and calculated V_{OC} losses values for different samples.

ACKNOWLEDGMENTS

This work was supported by the New Energy and Industrial Technology Development Organization (NEDO) under the Ministry of Economy, Trade, and Industry, Japan (METI).

The authors declare no conflict of interest.

DATA AVAILABILITY

The data that support the findings of this study are available within the article.

REFERENCES

- M. Nakamura, K. Yamaguchi, Y. Kimoto, Y. Yasaki, T. Kato, and H. Sugimoto, *IEEE J. Photovolt.* **9**, 1863 (2019).
- H.-W. Schock and R. Noufi, *Prog. Photovolt. Res. Appl.* **8**, 151 (2000).
- P. Paul, K. Aryal, S. Marsillac, S. Ringel, and A. Arehart, *Impact of the Ga/In Ratio on Defects in Cu(In, Ga)Se₂* (IEEE, 2016), p. 2246.
- T. Minemoto, Y. Hashimoto, W. Shams-Kolahi, T. Satoh, T. Negami, H. Takakura, and Y. Hamakawa, *Sol. Energy Mater. Sol. Cells* **75**, 121 (2003).
- R. Herberholz, V. Nadenau, U. Rühle, C. Köble, H. W. Schock, and B. Dimmler, *Sol. Energy Mater. Sol. Cells* **49**, 227 (1997).
- P. Jackson, D. Hariskos, R. Wuerz, W. Wischmann, and M. Powalla, *Phys. Status Solidi RRL* **8**, 219 (2014).
- F. Pianezzi, P. Reinhard, A. Chirila, B. Bissig, S. Nishiwaki, S. Buecheler, and A. N. Tiwari, *Phys. Chem. Chem. Phys.* **16**, 8843 (2014).
- Y. Sun, S. Lin, W. Li, S. Cheng, Y. Zhang, Y. Liu, and W. Liu, *Engineering* **3**, 452 (2017).
- P. Schöppe, S. Schönherr, R. Wuerz, W. Wisniewski, G. Martínez-Criado, M. Ritzer, K. Ritter, C. Ronning, and C. S. Schnohr, *Nano Energy* **42**, 307 (2017).
- A. Vilalta-Clemente, M. Raghuvanshi, S. Duguay, C. Castro, E. Cadel, P. Pareige, P. Jackson, R. Wuerz, D. Hariskos, and W. Witte, *Appl. Phys. Lett.* **112**, 103105 (2018).
- N. Taguchi, S. Tanaka, and S. Ishizuka, *Appl. Phys. Lett.* **113**, 113903 (2018).
- R. Wuerz, W. Hempel, and P. Jackson, *J. Appl. Phys.* **124**, 165305 (2018).
- S. Zahedi-Azad, M. Maiberg, and R. Scheer, *Prog. Photovolt. Res. Appl.* **28**, 1146–1157 (2020).
- D. Hauschild, D. Kreikemeyer-Lorenzo, P. Jackson, T. M. Friedlmeier, D. Hariskos, F. Reinert, M. Powalla, C. Heske, and L. Weinhart, *ACS Energy Lett.* **2**, 2383 (2017).
- S. Zahedi-Azad, M. Maiberg, R. Clausing, and R. Scheer, *Thin Solid Films* **669**, 629 (2019).

- ¹⁶T. Walter, R. Herberholz, C. Müller, and H. W. Schock, *J. Appl. Phys.* **80**, 4411 (1996).
- ¹⁷R. Herberholz, T. Walter, C. Müller, T. Friedlmeier, H. W. Schock, M. Saad, M. C. Lux-Steiner, and V. Alberts, *J. Appl. Phys. Lett.* **69**, 2888 (1996).
- ¹⁸J. A. M. AbuShama, S. W. Johnston, R. S. Crandall, and R. Noufi, *J. Appl. Phys. Lett.* **87**, 123502 (2005).
- ¹⁹T. Hölscher, T. Walter, T. Schneider, M. Maiberg, and R. Scheer, *Thin Solid Films* **669**, 345 (2019).
- ²⁰F. Werner, M. H. Wolter, S. Siebentritt, G. Sozzi, S. Di Napoli, R. Menozzi, P. Jackson, W. Witte, R. Carron, E. Avancini, T. P. Weiss, and S. Buecheler, *Prog. Photovolt. Res. Appl.* **26**, 911 (2018).
- ²¹U. Rau and H. W. Schock, *Appl. Phys. A Mater. Sci. Process.* **69**, 131 (1999).
- ²²J. T. Heath, J. D. Cohen, and W. N. Shafarman, *J. Appl. Phys.* **95**, 1000 (2004).
- ²³F. Werner and S. Siebentritt, *Phys. Rev. Appl.* **9**, 054047 (2018).
- ²⁴T. Eisenbarth, T. Untold, R. Caballero, C. A. Kaufmann, and H.-W. Schock, *J. Appl. Phys.* **107**, 034509 (2010).
- ²⁵O. Gunawan, T. K. Todorov, and D. B. Mitzi, *Appl. Phys. Lett.* **97**, 233506 (2010).
- ²⁶R. Scheer, *J. Appl. Phys.* **105**, 104505 (2009).
- ²⁷V. Nadenau, U. Rau, A. Jasenek, and H. W. Schock, *J. Appl. Phys.* **87**, 584 (2000).
- ²⁸J. Li, D. Wang, X. Li, Y. Zeng, and Y. Zhang, *Adv. Sci.* **5**, 1700744 (2018).
- ²⁹S. Ishizuka, H. Shibata, J. Nishinaga, Y. Kamikawa, and P. J. Fons, *Appl. Phys. Lett.* **113**, 063901 (2018).
- ³⁰D. V. Lang, *J. Appl. Phys.* **45**, 3023 (1974).
- ³¹T. Sakurai, H. Uehigashi, M. M. Islam, T. Miyazaki, S. Ishizuka, K. Sakurai, A. Yamada, K. Matsubara, S. Niki, and K. Akimoto, *Thin Solid Films* **517**, 2403 (2009).
- ³²S. Siebentritt, E. Avancini, M. Bär, J. Bombsch, E. Bourgeois, S. Buecheler, R. Carron, C. Castro, S. Duguay, and R. Félix, *Adv. Energy Mater.* **10**, 1903752 (2020).
- ³³A. Hierro, D. Kwon, S. A. Ringel, S. Rubini, E. Pelucchi, and A. Franciosi, *J. Appl. Phys.* **87**, 730 (2000).
- ³⁴H. Guthrey, A. Norman, J. Nishinaga, S. Niki, M. Al-Jassim, and H. Shibata, *ACS Appl. Mater. Interfaces* **12**, 3150–3160 (2020).
- ³⁵T. Sakurai, M. M. Islam, H. Uehigashi, S. Ishizuka, A. Yamada, K. Matsubara, S. Niki, and K. Akimoto, *Sol. Energy Mater. Sol. Cells* **95**, 227 (2011).
- ³⁶T. Meyer, F. Engelhardt, J. Parisi, and U. Rau, *J. Appl. Phys.* **91**, 5093 (2002).
- ³⁷S. Iany and A. Zunger, *J. Appl. Phys.* **100**, 113725 (2006).
- ³⁸M. Malitckaya, H.-P. Komsa, V. Havu, and M. J. Puska, *J. Phys. Chem. C* **121**, 15516 (2017).
- ³⁹N. Nicoara, R. Manaligod, P. Jackson, D. Hariskos, W. Witte, G. Sozzi, R. Menozzi, and S. Sadewasser, *Nat. Commun.* **10**, 3980 (2019).
- ⁴⁰M. I. Alonso, M. Garriga, C. D. Rincón, E. Hernández, and M. León, *Appl. Phys. A Mater. Sci. Process.* **74**, 659 (2002).
- ⁴¹M. Maiberg and R. Scheer, *J. Appl. Phys.* **116**, 123710 (2014).
- ⁴²W. K. Metzger, I. L. Repins, M. Romero, P. Dippo, M. Contreras, R. Noufi, and D. Levi, *Thin Solid Films* **517**, 2360 (2009).
- ⁴³D. Kuciauskas, I. Repins, A. Kanevce, J. V. Li, P. Dippo, and C. L. Beall, *Sol. Energy Mater. Sol. Cells* **136**, 100 (2015).
- ⁴⁴J. V. Li, S. Grover, M. A. Contreras, K. Ramanathan, D. Kuciauskas, and R. Noufi, *Sol. Energy Mater. Sol. Cells* **124**, 143 (2014).
- ⁴⁵T. Sakurai, K. Taguchi, M. M. Islam, S. Ishizuka, A. Yamada, K. Matsubara, S. Niki, and K. Akimoto, *Jpn. J. Appl. Phys.* **50**, 05FC01 (2011).
- ⁴⁶J. Werner, J. Mattheis, and U. Rau, *Thin Solid Films* **480–481**, 399 (2005).
- ⁴⁷U. Rau, B. Blank, T. C. M. Müller, and T. Kirchartz, *Phys. Rev. Appl.* **7**, 044016 (2017).

Supplementary material

Study of Defect properties and Recombination Mechanism in Rubidium Treated Cu(In, Ga)Se₂ Solar Cells

Hamidou Tangara,¹ Setareh Zahedi-Azad,² Jennifer Not,³ Jakob Schick,² Alban Lafuente Sampietro,¹ Muhammad Monirul Islam,^{1,4} Roland Scheer,² and Takeaki Sakurai^{1,a)}

¹Institute of Applied Physics, University of Tsukuba, Ibaraki 305-8573, Japan

²Institute of Physics, Martin-Luther-Universität Halle-Wittenberg, 06120 Halle, Germany

³Polytech Grenoble, Université Grenoble Alpes, 38400 Saint-Martin-d'Hères, France

⁴Alliance for Research on the Mediterranean and North Africa (ARENA), University of Tsukuba, Ibaraki 305-8573, Japan

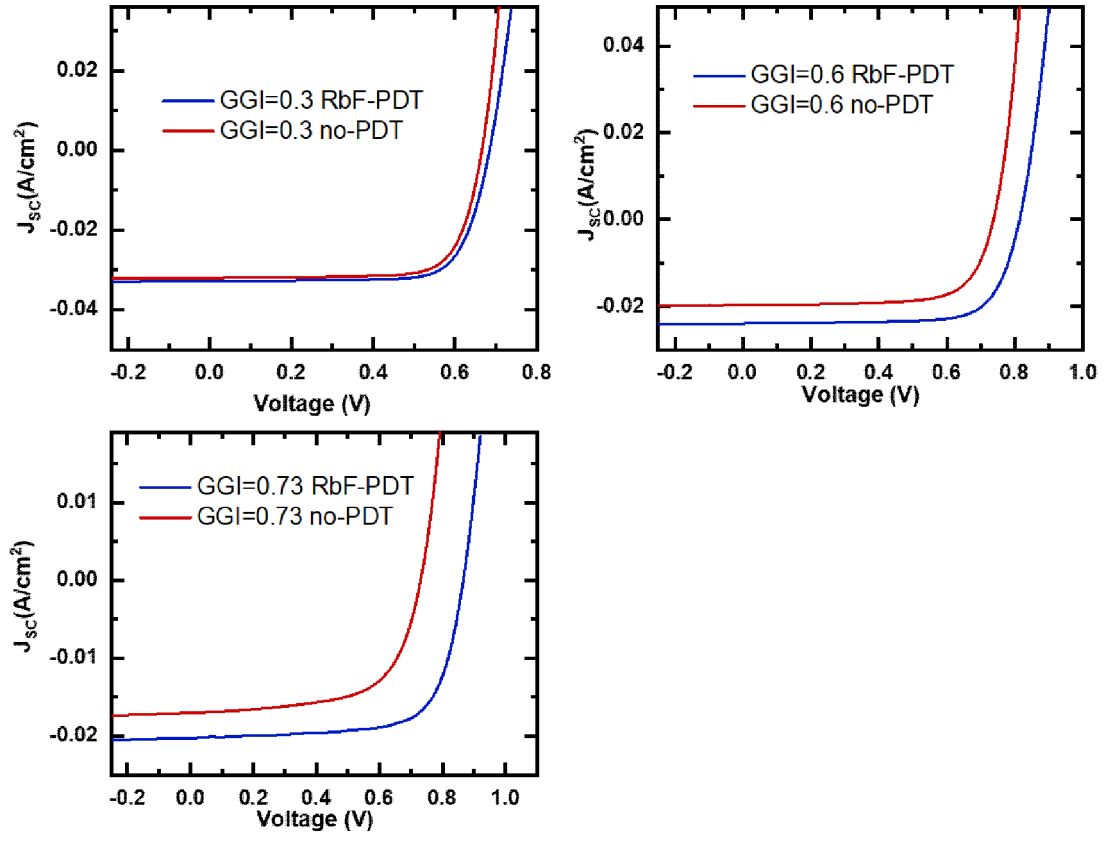


FIG. S1. J-V characteristics of the different samples shown in TABLE I.

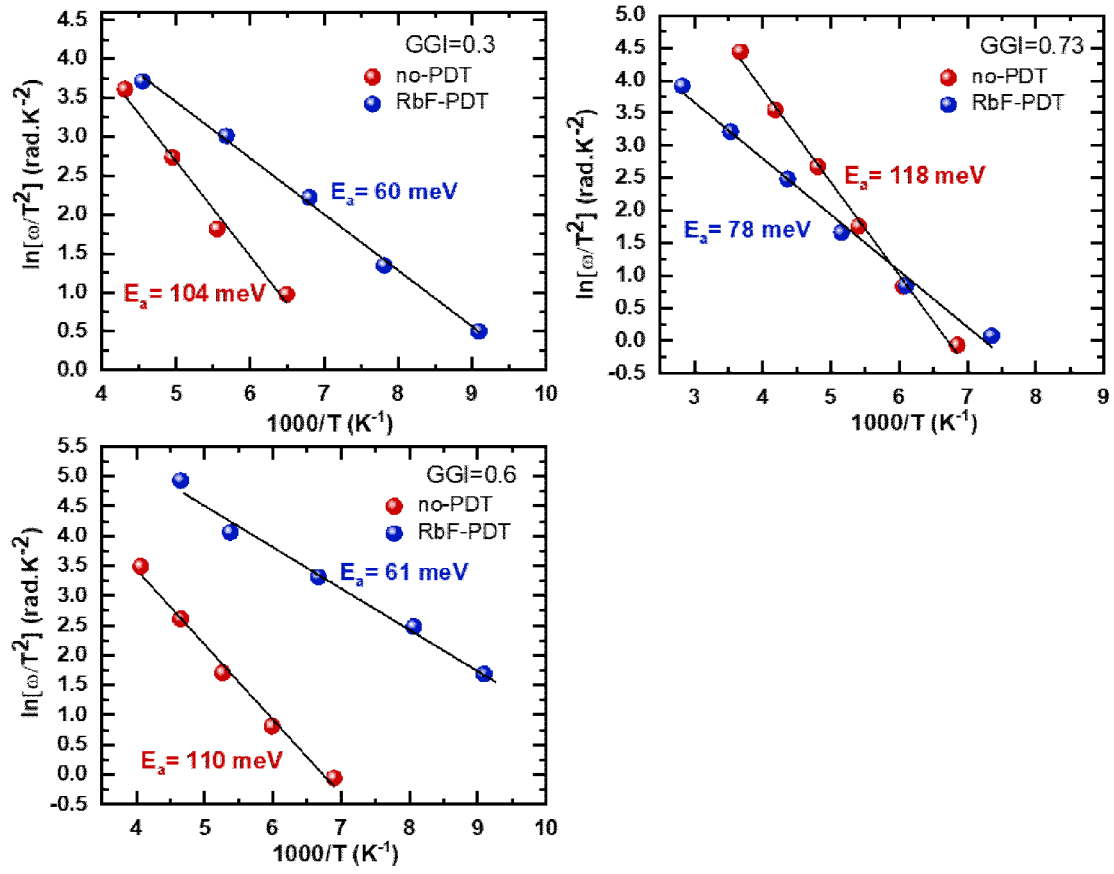


FIG. S2.(a)-(c) Arrhenius plots of characteristic frequencies obtained from admittance spectra of CIGSe solar-cells with different Ga content; GGI0.30, 0.60, and 0.73 before (no-PDT) and after RbF-PDT

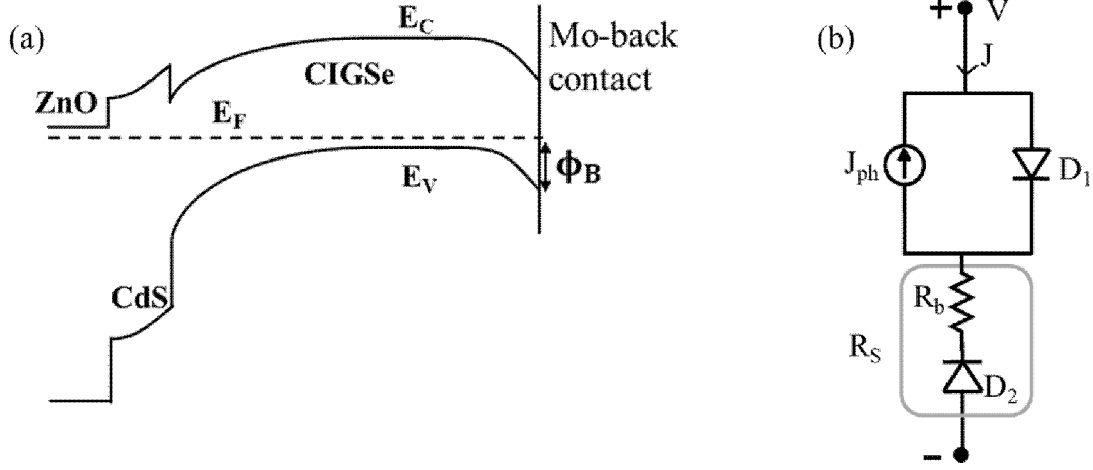


FIG S3(a)CIGSe band diagram with a Schottky contact with a height Φ_B at the CIGSe/Mo back contact, (b) Equivalent circuit describing the double-diode behavior due to the Schottky barrier.

The barrier height corresponds to the difference between the equilibrium Fermi level (E_F) and the valence band minimum (E_V) at the Mo metal surface. The equivalent circuit consists of two diodes with opposite polarity;²⁵ the main diode (D_1), which is located at the CdS/CIGSe interface, and the back contact diode (D_2) at the Mo/CIGSe interface. J_{ph} represents the photocurrent source. R_b denotes series resistance which is composed of D_2 and background series resistance R_0

When D_1 is forward biased, D_2 is in reverse bias and the back diode conduction is limited by its reverse saturation current which diminished rapidly at lower temperature resulting in an increase of the series resistance.

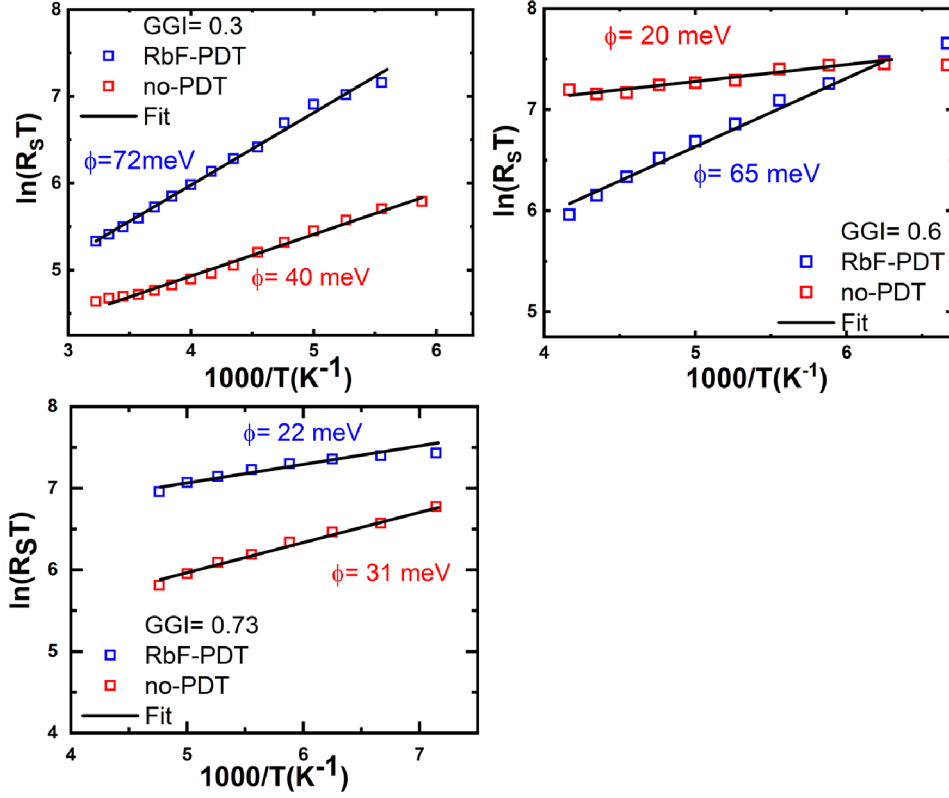


FIG. S4
samples
determin

o-PDT)
were

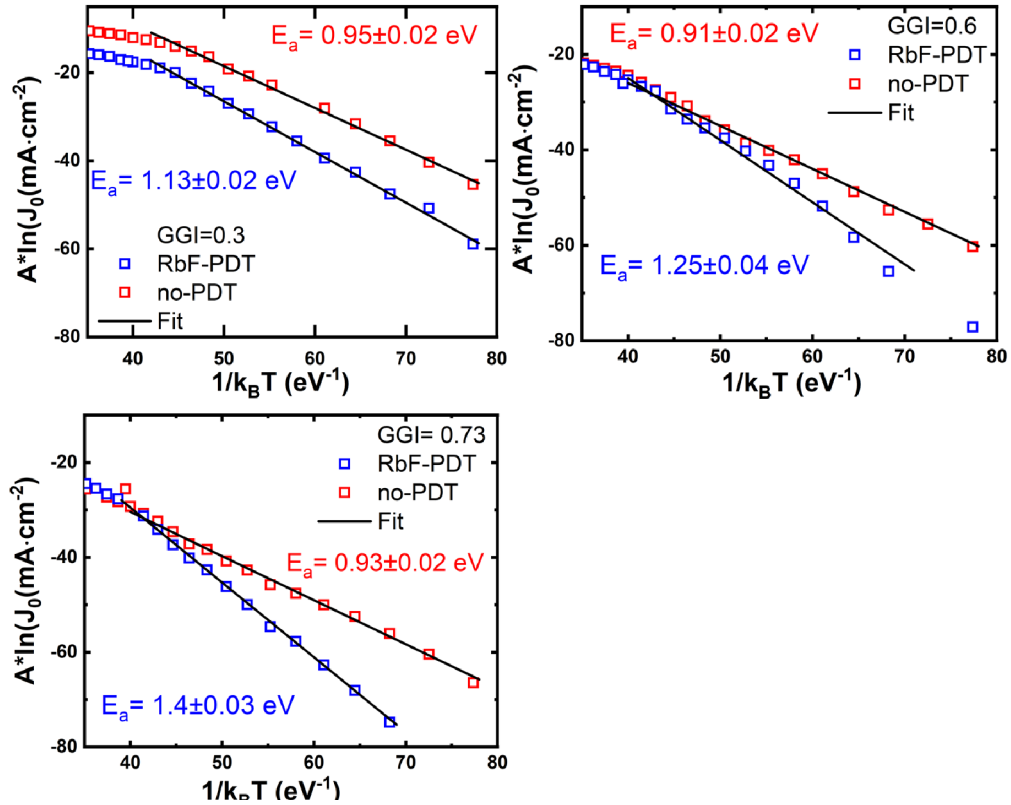


FIG. S5. Activation energy of of RbF-treated (RbF-PDT) and untreated (no-PDT) samples with different Ga content

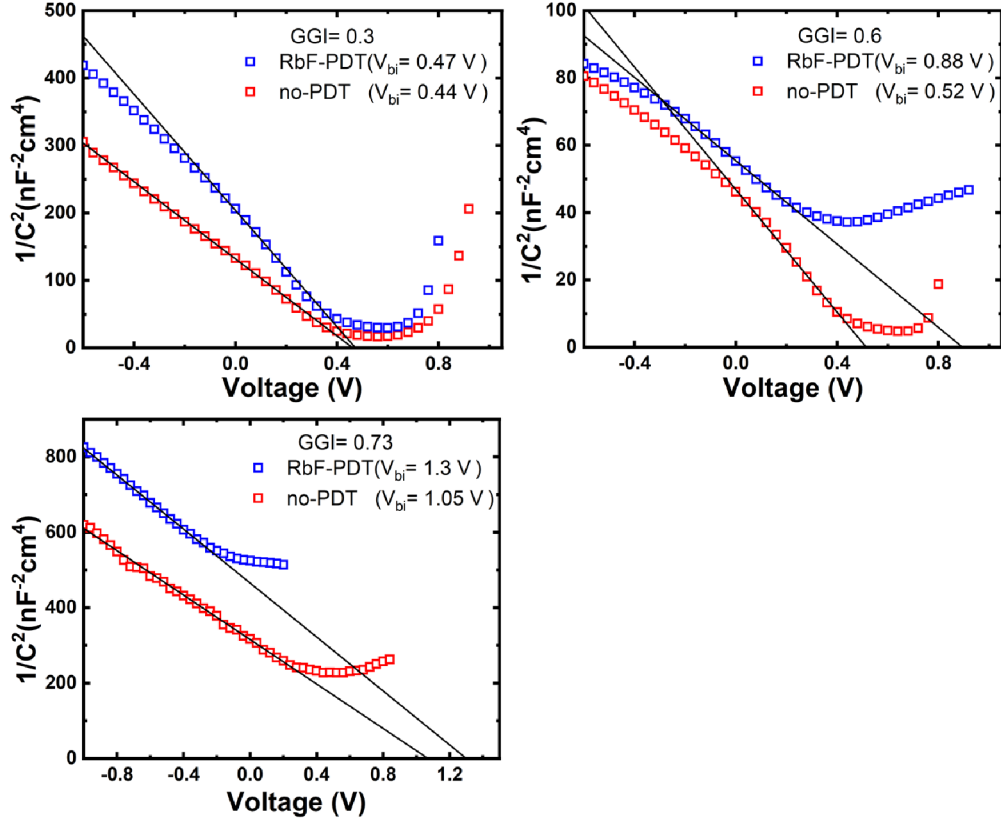


FIG. S6
Schottky
after Rb

3/CIGSe
DT) and

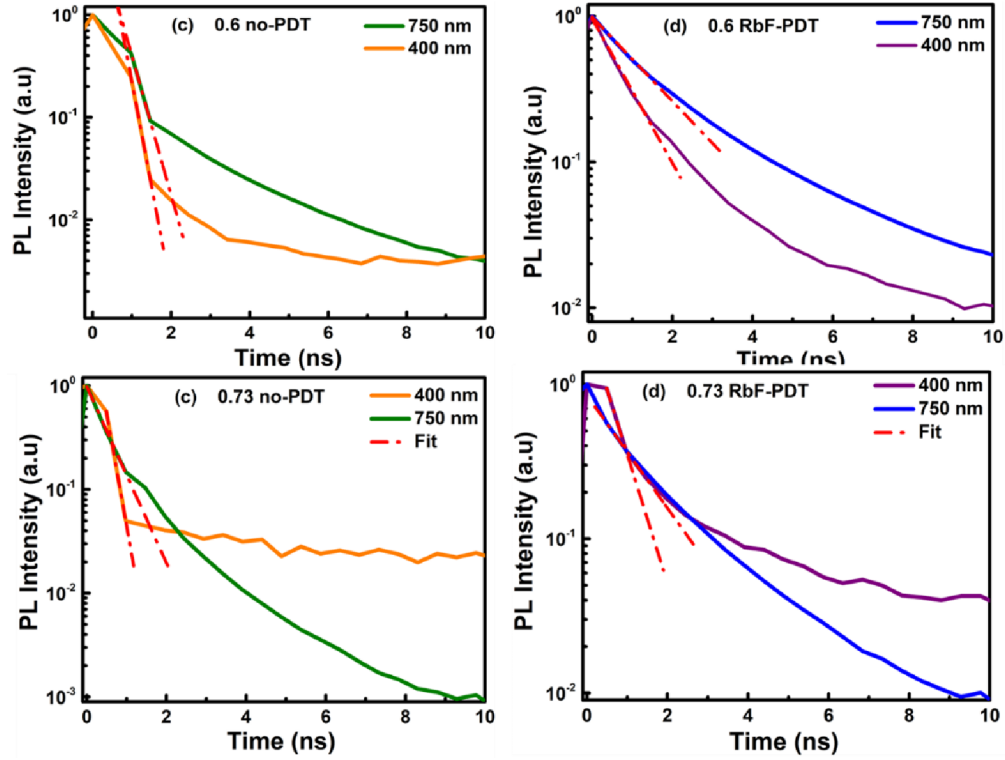


FIG. S7. Changes in the fast decay times of the different wavelengths in the first 10 ns for the untreated (c) and the treated (d) samples with GGI = 0.6 and 0.73

TABLE S1 Time constants extracted from a double exponential fit to the measured TRPL decay for CIGSe samples with different Ga content, GGI of 0.3, 0.60, and 0.73 before and after rubidium treatment at excitation wavelengths of 750 and 400 nm.

		0.30		0.60		0.73	
		no-PDT	RbF-PDT	no-PDT	RbF-PDT	No-PDT	RbF-PDT
750 nm	τ_1 (ns)	10	12	1.6	4.4	1.3	4
	τ_2 (ns)	39	50	5.6	18	7	20
400 nm	τ_1 (ns)	8.3	10.3	0.2	1.4	0.15	1.1
	τ_2 (ns)	36.7	53.4	7	19	20	25

TABLE S2 Intrinsic carrier density n_i , effective carrier density N_A , radiative recombination constants B and ideal carrier lifetime $\tau_{\text{rad, ideal}}$ for different samples before and after Rubidium treatment. The values of N_A were extracted from C-V measurements.

Ga content	n_i (cm ⁻³)		N_A (cm ⁻³)		B (cm ⁻³ s ⁻¹)		$\tau_{\text{rad, ideal}}$ (μs)	
	No-PDT	RbF-PDT	No-PDT	RbF-PDT	No-PDT	RbF-PDT	No-PDT	RbF-PDT
0.30	4.7×10^8		5×10^{15}	1×10^{16}	6.4×10^{-11}		2.6	1.3
0.60	1.7×10^7		5.4×10^{15}	1.5×10^{16}	1.6×10^{-10}		1.2	0.4
0.73	1.8×10^6		4.2×10^{15}	5×10^{15}	1.05×10^{-10}		2.3	2

TABLE. S3 Estimated ideal saturation current $J_{0, \text{ideal}}$ and saturation current in non-ideal case ($J_{0, \text{rad}}$) and the subsequent VOC loss due to nonradiative recombination (ΔV_{OC}). The improvement is obtained from the difference between the ΔV_{OC} before and after rubidium treatment.

Ga content	$J_{0, \text{ideal}}$ (A.cm ⁻²)		$J_{0, \text{rad}}$ (A.cm ⁻²)		ΔV_{OC} (mV)		Improvement
	No-PDT	RbF-PDT	No-PDT	RbF-PDT	No-PDT	RbF-PDT	
0.30	7.8×10^{-17}		5.2×10^{-15}	2.0×10^{-15}	-109	-84	25 mV
0.73	1.5×10^{-21}		4.9×10^{-18}	1.4×10^{-19}	-150	-118	136 mV